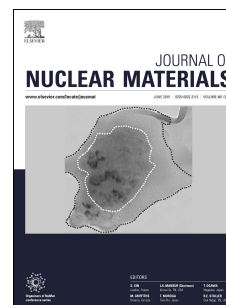


Accepted Manuscript

Microstructure, mechanical properties and strengthening mechanisms of friction stir welded Kanthal APMT™ steel

Anumat Sittiho, Vedavyas Tungala, Indrajit Charit, Rajiv S. Mishra



PII: S0022-3115(18)30417-3

DOI: [10.1016/j.jnucmat.2018.07.001](https://doi.org/10.1016/j.jnucmat.2018.07.001)

Reference: NUMA 51060

To appear in: *Journal of Nuclear Materials*

Received Date: 23 March 2018

Revised Date: 28 June 2018

Accepted Date: 2 July 2018

Please cite this article as: A. Sittiho, V. Tungala, I. Charit, R.S. Mishra, Microstructure, mechanical properties and strengthening mechanisms of friction stir welded Kanthal APMT™ steel, *Journal of Nuclear Materials* (2018), doi: 10.1016/j.jnucmat.2018.07.001.

This is a PDF file of an unedited manuscript that has been accepted for publication. As a service to our customers we are providing this early version of the manuscript. The manuscript will undergo copyediting, typesetting, and review of the resulting proof before it is published in its final form. Please note that during the production process errors may be discovered which could affect the content, and all legal disclaimers that apply to the journal pertain.

Microstructure, Mechanical Properties and Strengthening Mechanisms of Friction Stir Welded Kanthal APMTTM Steel

Anumat Sittiho^a, Vedavyas Tungala^b, Indrajit Charit^{a,1} and Rajiv S. Mishra^b

^a Chemical and Materials Engineering, University of Idaho, Moscow, ID 83844, USA

^b Materials Science & Engineering, University of North Texas, Denton, TX 76203, USA

Abstract

Kanthal APMTTM steel (Fe-22Cr-5Al-3Mo) is being investigated for possible use as an accident-tolerant fuel cladding material in advanced light water reactors. Generally, high-chromium ferritic steels do not have good weldability because of a variety of metallurgical issues. In the present study, friction stir welding (FSW), a solid-state joining process, was applied to a Kanthal APMTTM plate in a bead-on-plate configuration using a tool rotation rate of 600 RPM and a traverse speed of 25.4 mm/min. Microstructure and mechanical properties were evaluated to determine the weld quality and examine feasibility of applying FSW as a joining technique for this steel. Microstructural characteristics were examined by optical microscopy and electron microscopy. The stir zone (SZ) contained equiaxed grain structure with an average grain size of 13.7 μm . Interestingly, Vickers microhardness profile across the processed zone revealed no significant change in microhardness. Mini-tensile testing, however, showed a marked improvement in mechanical properties of the SZ in the longitudinal direction compared to the base metal. The results are discussed in the light of fundamental strengthening mechanisms.

Keywords: Friction Stir Welding/Processing; Ferritic Steels; Kanthal APMTTM; Accident-Tolerant Ferritic Steel

1. Introduction

Since the Fukushima-Daiichi nuclear disaster in 2011, efforts are ongoing to develop accident tolerant fuels and cladding materials for use in light water reactors. During the accident, water became steam due to high temperatures, which then reacted with zirconium based cladding alloys used in the boiling water reactors forming significant amount of hydrogen gas, ultimately leading to huge explosions among other outcomes. That is why there is a great interest in finding alternative cladding materials for light water reactors (LWRs), which can provide greater safety margins in the event of such accidents. One of the potential accident tolerant materials being considered for such applications is the aluminum-bearing ferritic steels [1-3].

¹ Corresponding author. I. Charit (e-mail: icharit@uidaho.edu; phone: +1-208-885-5964)

In high temperature applications, conventional chromium-bearing stainless steels having the passive chromia surface film for protecting the material underneath, is not able to offer high-temperature oxidation resistance when the service temperature rises above 1100 °C. On the other hand, alumina film-forming stainless steels have unique advantages over conventional stainless steels at high temperature under oxidizing environment because the α -alumina film is impermeable, stable, and slow-growing at temperatures beyond 1100 °C. FeCrAl steels are usually alloyed with more than 10 wt% Cr to slow down the growth rate of the protective α -alumina film [4]. Kanthal APMT™ is known as an alumina-forming, dispersion-strengthened ferritic stainless steel that is produced via powder metallurgy route [5]. This alloy is conventionally used for making structural elements of high temperature furnaces. Recently, there has been interest in using the alloy or alloys of similar compositions for possible accident-tolerant fuel cladding applications in advanced light water reactors [6]. Like other high-chromium dispersion-strengthened steels, APMT™ has difficulties with fusion welding techniques. The problems from fusion welding in high-chromium dispersion-strengthened ferritic steel are phase segregations, hydrogen attack, stress corrosion cracking, weld cracking, martensitic transformation, and loss of fine second phase particles [7,8]. Hence, developing enhanced weldability in these types of steels is of paramount importance.

Friction stir welding (FSW) is a solid-state welding technique involving a non-consumable tool plunging into the contact interface of the two plates while plastically deforming and mixing materials in its wake without melting the base metal [9]. Most of the heat during the FSW process is generated from the friction between the tool and the material surface, and some by adiabatic heating from severe plastic deformation of the material itself [10,11]. The tool pin stirs and transfers material from the advancing side, where the tool rotates toward the tool traverse movement, to the retreating side where the tool rotation and traverse directions are opposite. Until now, FSW has been successfully applied to various types of metallic materials, such as aluminum alloys, magnesium alloys, nickel-based superalloys, titanium alloys, and steels. Specifically, FSW has also been used for joining high chromium steels [12-14] and oxide dispersion strengthened (ODS) alloys [8, 15-17]. No previous study applied FSW to Kanthal APMT™ except one by Grant and Weil at the Pacific Northwest National Laboratory [18]. Their work presented a preliminary assessment of high temperature mechanical property (creep strength) of FSW APMT™. Recently, the present authors published some preliminary findings on the FSW of APMT™ [19]; however, neither the microstructure evolution due to FSW nor the strengthening mechanisms was studied in detail. Hence, the objective of the present study is to make a detailed assessment of the feasibility of FSW application for APMT™. The scope of the study involves examination of changes in microstructural features using optical microscopy and electron microscopy, and evaluation of resulting

mechanical properties via Vickers microhardness and tensile testing. Finally, the results obtained are elucidated in the light of existing strengthening mechanisms.

2. Experimental procedure

2.1 Material and Processing

A Kanthal APMT™ plate (100 mm × 610 mm × 8 mm) was procured from Sandvik Heating Technology, Hallstahammar, Sweden. The nominal composition (in wt%) of the as received APMT™ plate was Fe-22Cr-5Al-3Mo-0.05(max.)C-0.4(max.)Mn-0.7(max.)Si-0.1Y-0.02Ti-0.1Hf-0.5Zr. The as-received APMT™ plate was subjected to FSW in a bead-on-plate configuration. For welding feasibility studies, this kind of bead-on-plate runs is convenient over actual welding to examine associated metallurgical changes. The FSW tool used in this study was made of polycrystalline cubic boron nitride (PCBN) with a conical threaded pin. The dimensions of the tool used were as following: shoulder diameter of 25.0 mm, pin height of 5.0 mm, and pin diameter of 7.6 mm. FSW parameters used were the following: tool rotational rate of 600 RPM, traverse speed of 25.4 mm/min, and forging force of 21 kN. The peak temperature measured by a thermocouple located inside the spindle tool near the tool shoulder was recorded as approximately 1000 °C. The associated FSW temperature profile is shown in Figure 1.

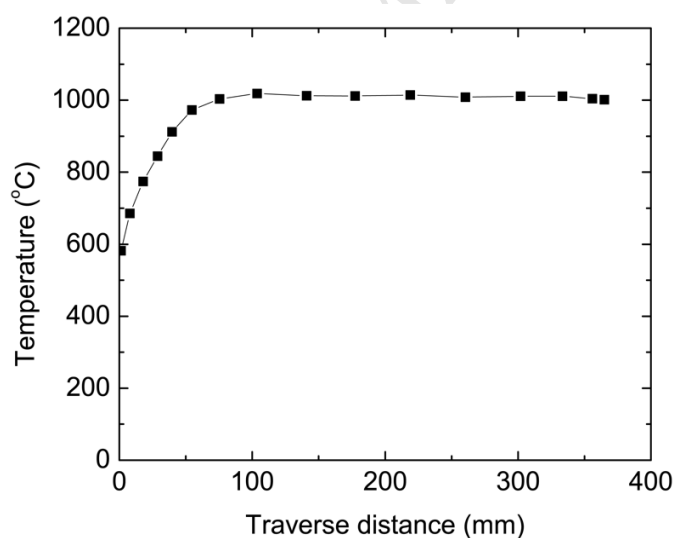


Figure 1. Temperature vs. tool traverse distance during FSW of the APMT™ plate.

2.2 Microstructural study

2.2.1 Optical microscopy

The FSWed APMT™ plate was sectioned using a diamond wafering blade along the transverse direction to create a few short pieces for further examination. The specimen then mounted in Bakelite using Pace Technologies Terapress hot mounting machine. The grinding and polishing of the mounted

samples were performed using Allied HighTech Twinprep-3TM machine. Grinding steps were performed on SiC grinding papers and polished using polycrystalline diamond suspension down to 0.05 μm , followed by thorough surface cleaning in the ultrasonic cleaner to give a mirror-finish for the metallographic specimens. Subsequently, the polished specimens were chemically etched with Glyceregia etchant (nitric acid:hydrochloric acid:glycerol = 1:3:2, by volume) for 3 minutes. Optical microscopy was carried out using an Olympus PMG-3 inverted metallurgical microscope.

2.2.2 Electron microscopy

Thin slices were sectioned from the base material (BM) and the stir zone (SZ). Then, they were ground down to a thickness of 60-150 μm and punched into standard 3-mm diameter discs. Then the specimens were subjected to twin-jet electropolishing by using Fischione model 110 twin-jet electropolisher. A solution of 15% HNO_3 and 85% methanol (by volume) was used in electro-jet polishing; the parameters used were: potential of 25 V and temperature range between -40 $^{\circ}\text{C}$ to -50 $^{\circ}\text{C}$. Finished specimens were examined with JEOL 2010 transmission electron microscope (TEM) operated at 200 kV. The TEM was equipped with an energy dispersive x-ray spectroscopy (EDS) system. Statistically significant results comprising size, number density, and volume fraction of the dispersed second phase particles were obtained from several random areas of each region. The measurement followed the method described by Higginson and Sellars [20]. Convergent beam electron diffraction (CBED) technique was used to determine the thickness of the regions of interest in the TEM samples, necessary for calculating the particle volume fractions [21].

The carbon extraction replica technique was used to analyze the chemical composition of the second phase particles to minimize the 'matrix effect'. A polished specimen was heavily etched followed by application of a thick carbon coating by using the vacuum evaporation method. After the carbon film was deposited on the etched surface, the sample was etched again to corrode the substrate beneath and extract the carbon film for further examination in a Zeiss Supra 35 Field Emission Gun (FEG) scanning electron microscope (SEM) and to perform EDS studies.

Electron back-scatter diffraction method (EBSD) was used to study the grain boundary misorientation distributions within the BM and SZ regions. In order to create the necessary distortion-free surface for EBSD, discs of 300 μm thickness and 3 mm diameter made from both BM and SZ were subjected to electro-jet polishing using the same parameters as the TEM specimens as described previously in this section. The Thermofisher Scientific QuasorTM EBSD system available with the Zeiss Supra 35 FEG SEM operated was used at an accelerating voltage of 10 kV.

2.3 Evaluation of Mechanical Properties

2.3.1 Vickers microhardness testing

To measure Vickers microhardness across the transverse cross-section of the stir zone, the etched optical metallography specimen was re-polished to make the surface smooth, and subsequently Vickers microhardness testing was performed under a load of 0.5 kgf (4.91 N) and dwell time of 15 s by using a LECO LM100 Vickers microhardness tester. The microhardness profiles were generated at the depths of 1, 2, and 3 mm along the horizontal direction below the upper surface of the plate. The spacing between each successive indentation was kept at 1 mm. Further, microhardness testing on the same transverse cross-section along six vertical directions were performed covering the whole stir zone.

2.3.2 Tensile testing

In this study, tensile testing was done in two different ways, i.e. conventional tensile testing and mini-tensile testing. In conventional tensile testing, dog-bone shaped tensile specimens were machined in the transverse direction from the FSWed plate in the configuration as shown in Figure 2. Tensile specimens with the gauge length of 30 mm, 3.5 mm gauge width and 1.34 mm thickness) were machined to completely include all the characteristic regions including the SZ within the gauge section. These tests were performed using an Instron 5982 universal tester. Mini-tensile testing was also used for studying tensile properties from the SZ and the BM. The tensile specimens for mini-tensile testing were machined to have a gauge length of 2 mm, 1 mm width and 0.5 mm thickness. A custom-made mini-tensile tester was used under the same testing parameters as the conventional tensile testing. The displacement data from the tensile tests were obtained from the instrument crosshead movement rate. In order to avoid the ambiguity from the elastic displacement contributed by the instrument fixture, the elastic displacement of the system was subtracted from the total displacement to calculate the corresponding engineering plastic strains of the specimen, which were utilized in the construction of stress-strain plots. The same approach was used for the analysis of conventional tensile test results to maintain consistency. The conventional tensile tests were done on one specimen each from the BM (transverse direction) and bulk FSWed material (also transverse direction); so no error could be reported for these results. In contrast, mini-tensile testing was conducted on two specimens from each region, i.e. BM (longitudinal), SZ (longitudinal), and SZ (transverse), and thus the spread in mini-tensile properties could be reported. Following tensile testing, fracture surfaces of the tensile specimens were examined using a Zeiss Supra 35 FEG-SEM operated at accelerating voltages between 5 and 20 kV.

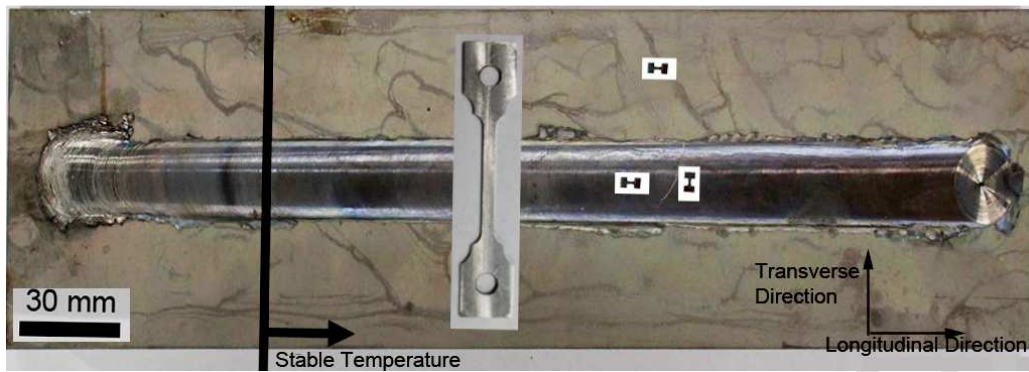


Figure 2. Views of the tensile specimens (both conventional and mini-tensile) overlaid on the FSWed APMT™ plate (bead-on-plate configuration).

3. Results

3.1 Optical microscopy

The optical macrograph in Figure 3 shows the microstructural gradient across the transverse cross section of the as-welded APMT™ plate. The sharp interface between the SZ and the thermomechanically affected zone (TMAZ) is observed on the advancing side, while on the retreating side it is slightly diffused. The as-received APMT™ plate (the parent material) consists of elongated, pancake-shaped grains as typical of hot rolled plates as shown in Figure 4. The mean linear intercept (MLI) method was used to measure the grain size, which is found to be $74 \pm 33 \mu\text{m}$. The difference in grain morphology in various regions of the SZ is revealed in the optical micrographs shown in Figure 5. The overall MLI grain size in the center of the SZ was determined to be $13.7 \pm 2.1 \mu\text{m}$. However, the grain sizes within the different regions of the SZ is found to be variable. The MLI grain size was 17.2 ± 2.0 and $16.1 \pm 1.1 \mu\text{m}$ at the center of the SZ in transverse direction and longitudinal direction, $16.7 \pm 3.3 \mu\text{m}$ at the retreating side, $13.6 \pm 1.7 \mu\text{m}$ at the advancing side, $9.7 \pm 1.5 \mu\text{m}$ and $11.3 \pm 2.1 \mu\text{m}$ at the top and bottom of the SZ, respectively. In TMAZ, the grain shape appeared elongated because of the nature of the material flow around the stir zone periphery. The SZ/TMAZ interface is more distinct on the advancing side than on the retreating side. The transition region between the TMAZ and the BM is distinguished by using deformed and non-deformed grain structure. The heat affected zone (HAZ) could not be detected by optical microscopy.

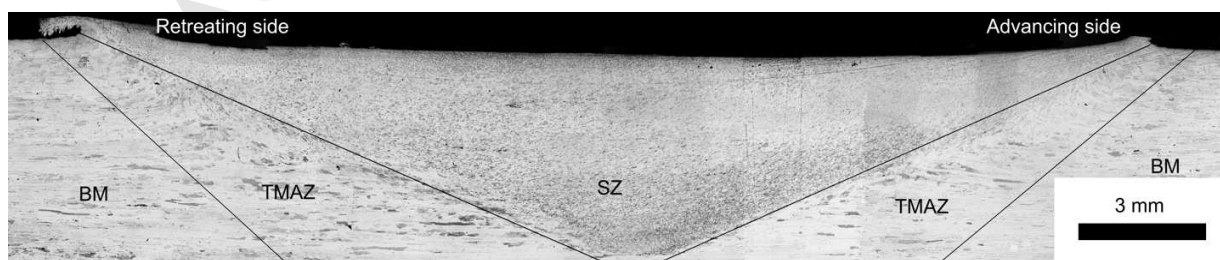


Figure 3. A collaged optical macrograph of the FSWed APMT™ plate showing the transverse cross section of the weld – adapted from ref. [19].

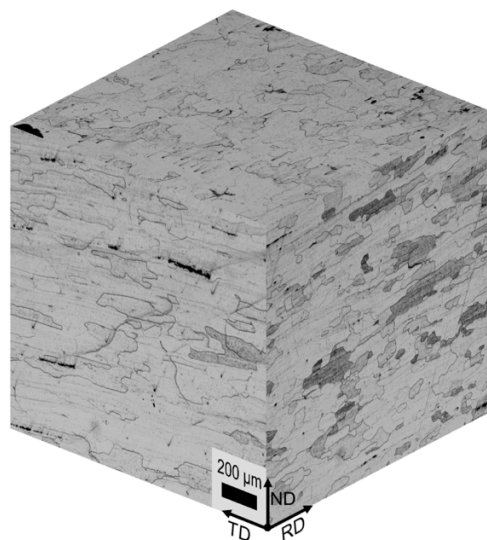


Figure 4. Three-dimensional optical micrograph of the as-received APMT™ plate.

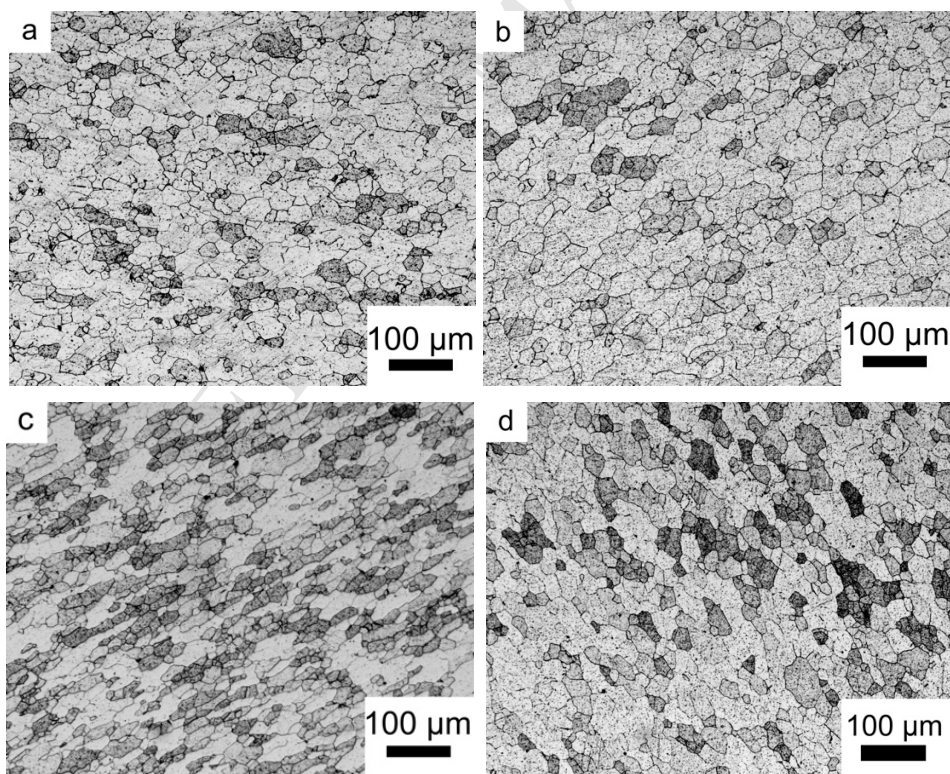
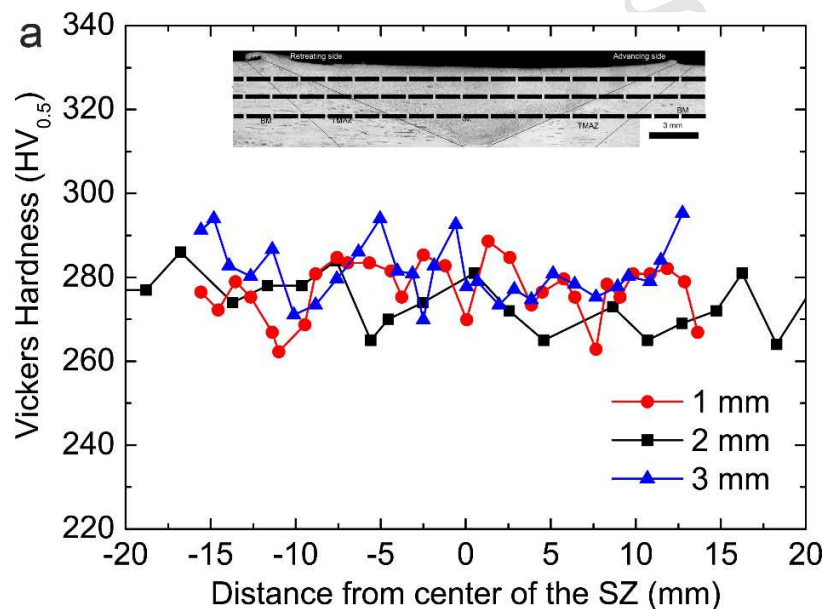


Figure 5. Optical micrographs of the FSWed APMT™ steel: a) retreating side, b) center of the stir zone (transverse), c) advancing side, and d) center of stir zone (longitudinal).

3.2 Microhardness profiles

The microhardness profiles taken along the horizontal direction of the FSWed APMTTM plate at different depths from the upper surface, as shown in Figures 6(a), exhibit no significant region-specific hardness changes across the weld. The mean Vickers microhardness across the weld is found to be 272 ± 7 HV_{0.5}. Typically, HAZ can be determined by the characteristic change in local hardness. However, in this study the microhardness profile shows no such change over any area. Thus, no HAZ could be detected unambiguously from the microhardness profiles of the FSWed specimen. Also, as shown in Figure 6(b) microhardness profiles along the vertical directions at various areas from the center of the SZ toward both the retreating side and the advancing side did not exhibit any significant hardness change.



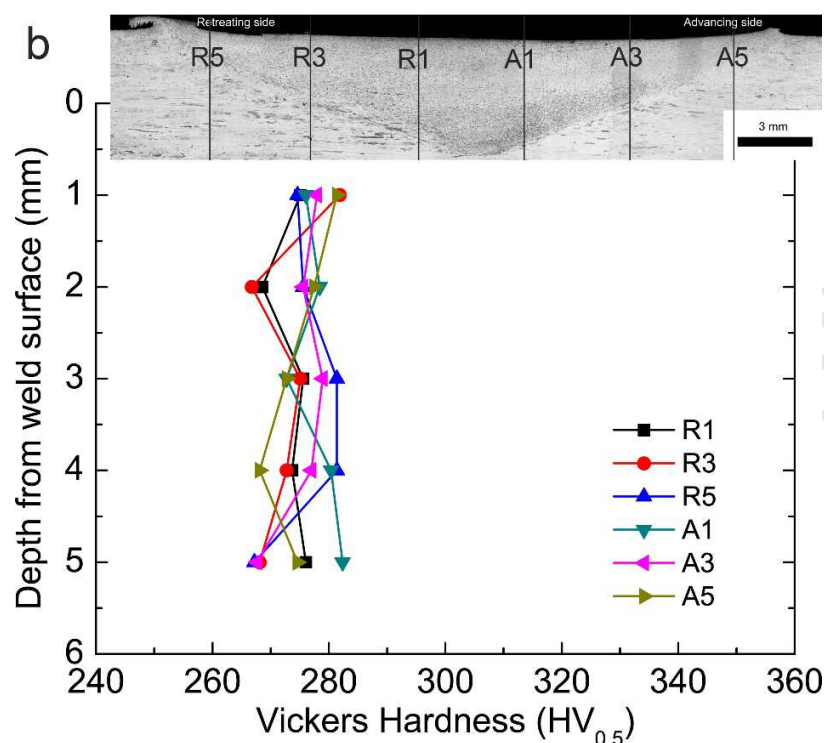


Figure 6. Vickers microhardness profiles measured on the transverse cross section of the FSWed APMTTM plate along a) the three horizontal directions and b) the six vertical directions of the weld.

3.3 Electron microscopy

TEM study on the APMTTM plate revealed a number of second phase particles. These dispersed particles are typically reported to be enriched in Y, (Hf, Zr), and Ti [22]. Figure 7(a) shows bright field TEM images of the BM. The microstructural features of the BM contain dislocations arrangements typical of a recovered state. The dislocation density in the BM is measured to be $4.7 \times 10^{12} \text{ m}^{-2}$. Figures 7(b) and (c) show a representative TEM image of the SZ. Some dispersoids are found to have coarsened and some degree of particle agglomeration is also evident. The measured dislocation density in the SZ is found to be lower ($2.4 \times 10^{12} \text{ m}^{-2}$) than that in the BM. The EDS study of the particles in both the BM and SZ showed that the larger particles are Y-rich and the smaller particles are rich in Hf and Zr. Because of the ‘matrix effect’, the exact particle compositions could not be determined from the EDS spectra using the conventional TEM samples.

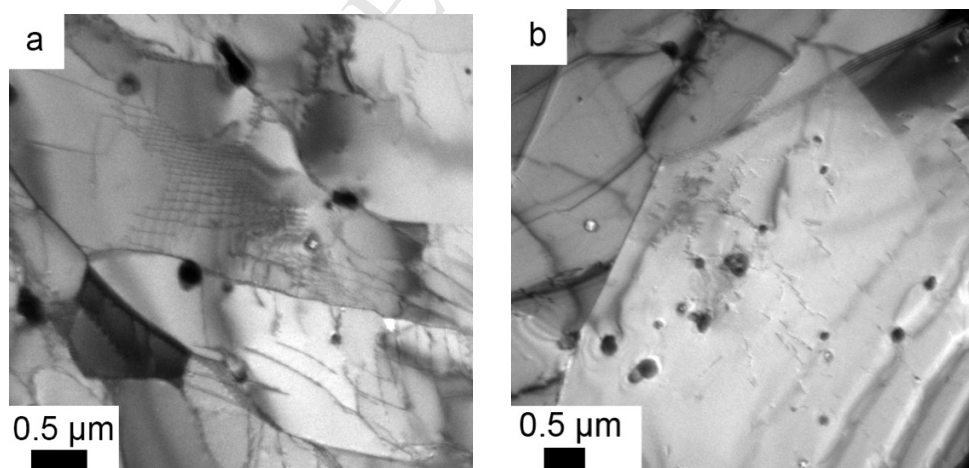
To address the above problem, carbon replica technique was used to isolate the particles from the BM matrix and then analyzed in SEM. The EDS spectra from 30 randomly selected particles were analyzed. Here also, EDS analyses detected mainly two types of particles as shown in the backscattered electron (BSE) SEM images of the corresponding carbon replicas (Figure 8). In Figure 8 (a) and (b)

insets, the EDS spectra of the particles (indicated by arrows) show the particles are rich in Hf-Zr (brighter contrast) and Y-Al (darker contrast). By using elemental ratio from the EDS spectra, the Hf-Zr rich particles are found to be $(\text{Hf,Zr})\text{O}_2$ and Y-Al rich particles are $\text{Y}_3\text{Al}_5\text{O}_{12}$ (yttrium aluminum garnet: YAG) type. The YAG particles are larger than the $(\text{Hf,Zr})\text{O}_2$ particles. Although $\text{Ti}(\text{C,N})$ particles are likely to be present in the specimen, EDS analyses of several particles did not reveal the presence of those types of particles.

The size and volume fraction of particles in the BM and the SZ of FSWed APMTTM are summarized in Table I. Histograms depicting particle size distributions of both the BM and SZ regions are shown in Figure 9. The distribution curve shifts to the right but maintains the skewed normal distribution. In the BM, the particles are found to have a mean diameter of 106 nm and volume fraction of 0.016. In the SZ, an average size of the second phase particles is 147 nm and volume fraction of 0.019. The smallest particle size in the BM is measured to be 30 nm while in the SZ the smallest particle diameter is found to be 60 nm.

Table I. Size and volume fraction of second phase particles in each region.

Regions	Mean diameter (nm)	Volume fraction
BM	106 ± 5	$0.016 \pm .003$
SZ	147 ± 26	$0.019 \pm .001$



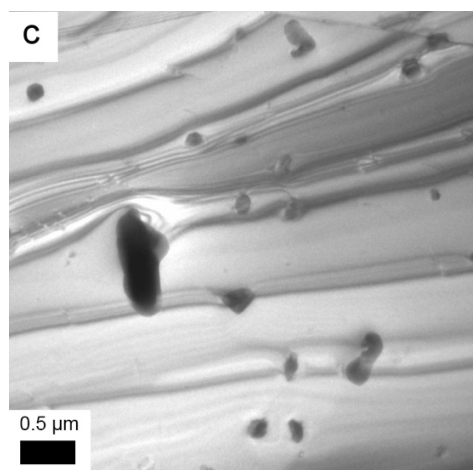


Figure 7. The BF-TEM micrograph from a) the BM, b) and c) the SZ.

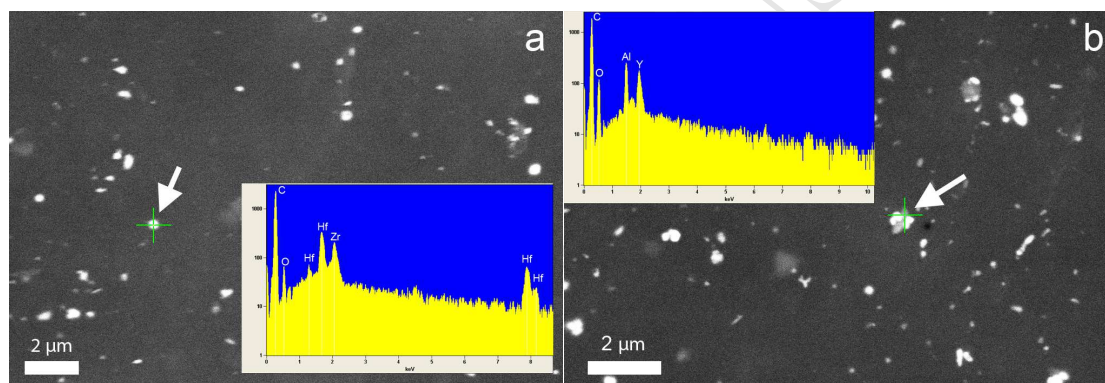


Figure 8. BSE-SEM micrographs of carbon replicas from the APMT™ plate (with the corresponding EDS spectra as inset) showing two different second phase particles: a) $(\text{Hf,Zr})\text{O}_2$ and b) $\text{Y}_3\text{Al}_5\text{O}_{12}$ (yttrium aluminum garnet).

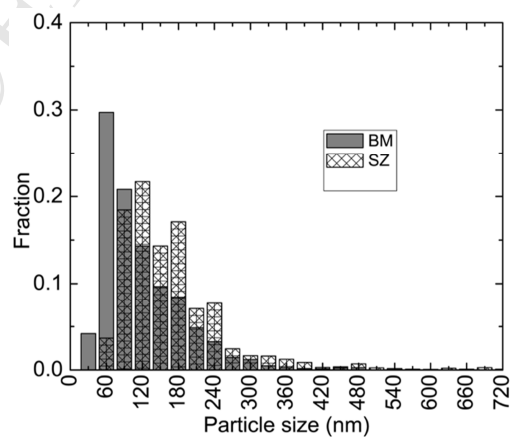


Figure 9. Particle size distributions in the BM and SZ of the FSWed APMT™ plate.

EBSD study revealed a difference between the grain boundary misorientation distributions of the BM and the SZ. Figure 10 shows the corresponding grain boundary misorientation distributions. Here the low angle grain boundary (LAGB) is defined as having grain boundary angles between 2° to 15° , and high angle grain boundary (HAGB) with misorientations greater than 15° . The proportion of LAGBs in the SZ is found to be lower (4%) than in the BM (10%).

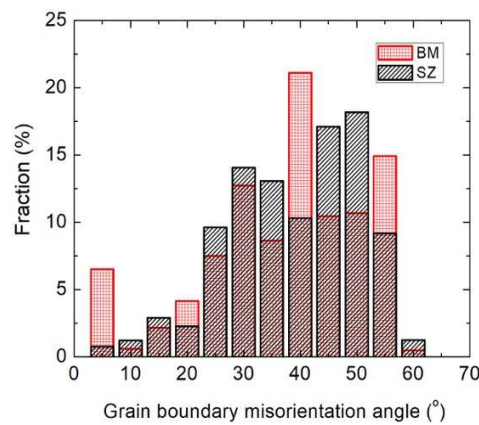


Figure 10. Grain boundary misorientation distribution histograms of APMT™ for both the BM and the SZ.

3.4 Tensile testing and fracture surface analysis

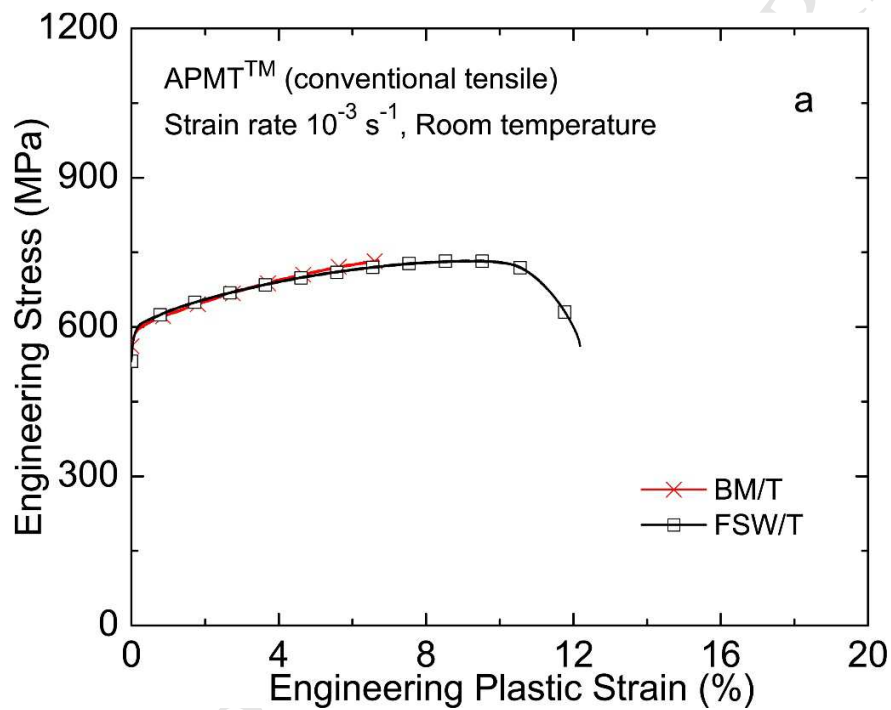
Standard tensile testing and mini-tensile testing results at room temperature show that FSW can improve mechanical properties of APMT™. The failure location of the full-length FSWed specimens was found to be just outside the SZ. Further, mini-tensile testing on specimens with gauge length fully within the SZ exhibited higher yield strength and ductility compared to the BM. The tensile properties thus obtained are listed in Table II.

Table II. Tensile properties of the base material and FSWed APMT™

Specimen	Yield strength (MPa)	Tensile strength (MPa)	Elongation (%)
BM-transverse ¹	594	735	6.6
BM-longitudinal ²	640±40	800±49	10±2.6
FSWed ¹	609	734	11.3
SZ-transverse ²	657±84	806±88	18±0.6
SZ-longitudinal ²	790 ±55	968±44	18±0.9

¹ conventional tensile testing, and ² mini-tensile testing

From Figure 11 (a), it can be found that the yield strength and tensile strength are comparable between the as-received (parent) material and FSWed specimens as obtained from the tensile testing of the full-length specimens. On the other hand, the mini-tensile test results demonstrate that the room temperature strength and ductility of the SZ region (in the longitudinal direction) are improved over those of the parent material tested in the same direction. Unfortunately, the mini-tensile data of the parent material in the transverse direction could not be obtained because of the lack of sufficient material.



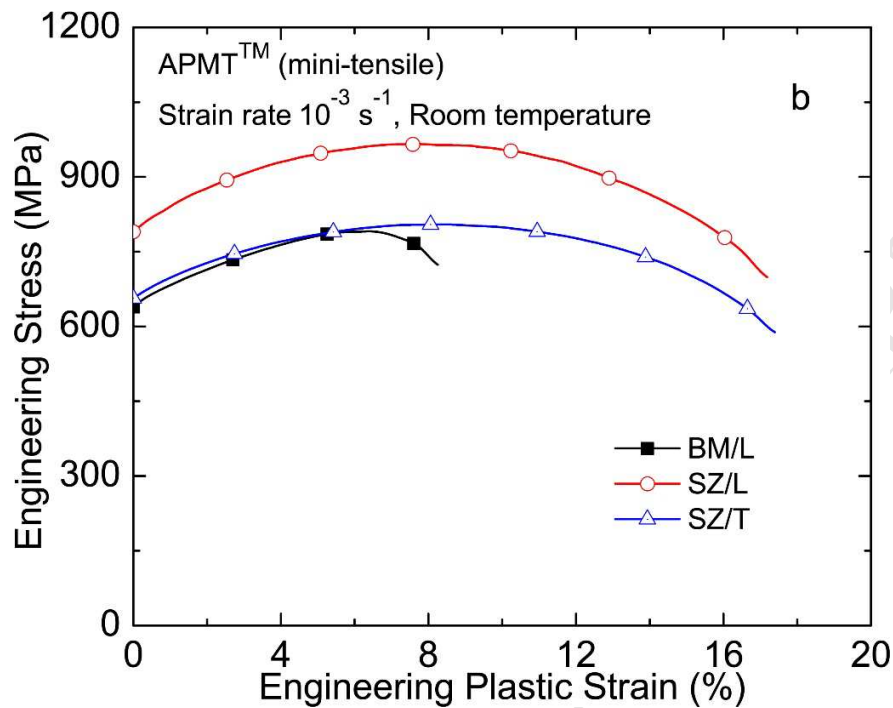


Figure 11. Engineering stress – engineering plastic strain curves of the as-received and FSWed APMT™ from a) full-length tensile specimen testing in the transverse direction (T); and b) mini-tensile specimen testing in both transverse (T) and longitudinal (L) directions.

The fractographic examination of the tensile tested specimens was conducted using secondary electron imaging mode in a SEM. Figure 12 (a) and (b) show SEM images of the fracture surfaces of the full-length tensile specimens for each condition. The fractographic images revealed brittle fracture in both as-received and FSWed conditions. In the FSWed specimen, the fracture occurred just outside the SZ. Figures 12 (c) and (d) depict the fracture surface of the mini-tensile testing specimens. Both images show ductile fracture type.

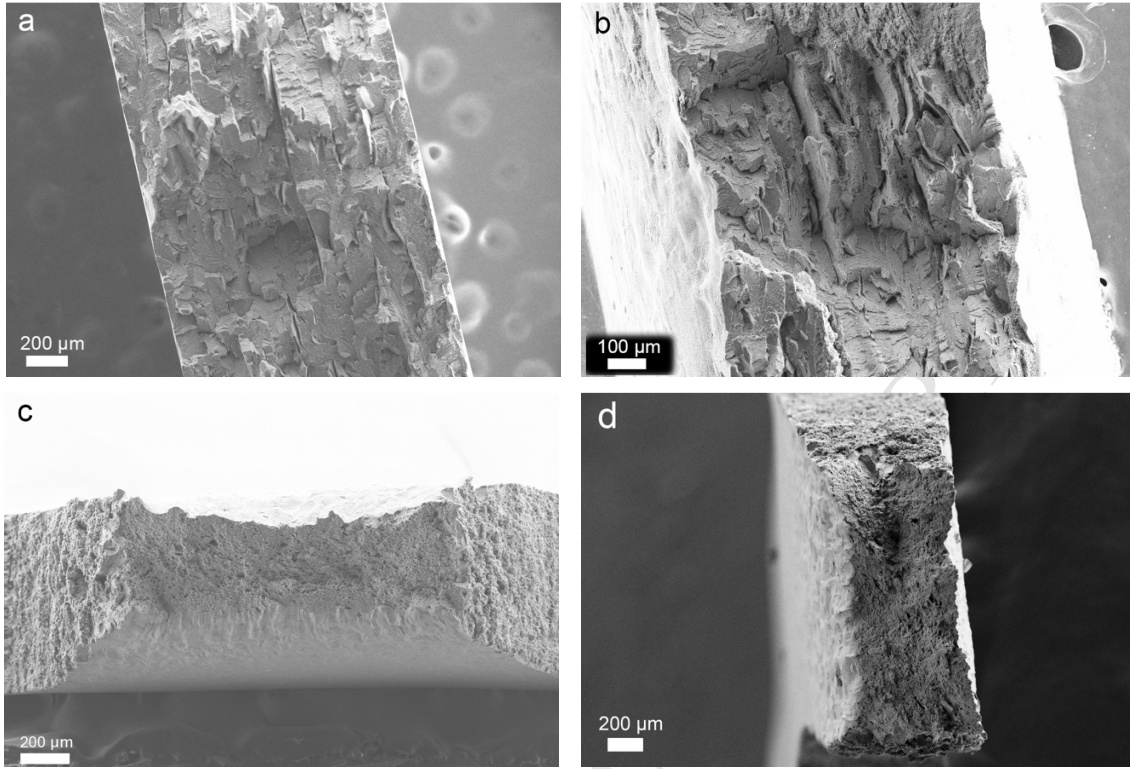


Figure 12. Secondary electron (SE) SEM images of fracture surfaces of the full-length tensile specimens for a) the base material and b) the FSWed APMT™. SE images of the mini-tensile tested specimens of the c) SZ in the transverse direction, and d) mini tensile testing of the SZ in the longitudinal direction.

4. Discussion

4.1 Microstructure evolution during FSW

The optical micrographs taken from various regions in the SZ have been shown in Figure 5. The grain size measurement revealed the difference in grain size within the SZ. The grain structure in the SZ is the result of dynamic recrystallization during FSW with smaller grain size and higher fraction of HAGB. As a result of the complexity of the FSW process such as temperature and material flow profiles, the grain sizes in each location in the SZ are different. The flow of material in FSW is analogous to hot extrusion process. The material is extruded through the confined area between the pin and the colder area of the material at the retreating side. The combined effect of the strain rate and temperature on the material plastic flow can be described by Zener-Hollomon parameter (Z) as shown in Equation (1) [23]. Ammouri *et al.* [24] utilized the empirical equation as Equation 2 for predicting the final grain size of FSW AZ31B alloy by using Z parameter.

$$Z = \dot{\epsilon} \exp(Q/RT) \quad (1)$$

and

$$d^{-1} = a + b \ln Z \quad (2)$$

where $\dot{\epsilon}$ is the strain rate, Q is the appropriate activation energy, R is the gas constant, T is the deformation temperature, d is grain diameter, and a and b are materials parameters. From Equations (1) and (2), higher strain rate and lower temperature lead to higher Z values, which result in smaller grain size. Since the material flow and heat distribution of FSW are rather complex, the computational techniques have been found to be helpful in studying the process [10, 11, 25].

A high amount of energy is imparted to the material during FSW through the heat generated from tool/specimen friction and severe plastic deformation. The known mechanisms in material to relieve the stored energy are recovery and recrystallization. The second phase particles evolve by coarsening to decrease the interfacial energy to their lower energy state. Generally, mechanisms governing the particle coarsening have been proposed to be the following: mechanically driven particle agglomeration [26], phase transformation [16, 27, 28], and kinetically driven Ostwald ripening [27, 28].

The particles identified are YAG and (Hf, Zr)O₂ type, both of which are thermally stable phases and are found in both BM and SZ. Thus, the particle coarsening by phase transformation is not a factor in this case. Ostwald ripening, kinetically driven particle coarsening mechanism, is a possible cause for the coarsening of dispersoids. Ostwald ripening involves dissolution of smaller particles, diffusion of those dissolved atoms, and further increase in the mean size of larger particles, leading to an increase in interparticle spacing [29]. The volume fraction of the particles remained more or less constant and the measured average interparticle spacing increased from 671 nm to 1028 nm. This quantitative study of the change in size, volume fraction, and interparticle study indicates some evidence of particle coarsening via the Ostwald ripening mechanism. Since Ostwald ripening is a kinetically controlled mechanism, the morphology of the coarsened particles would not necessarily change. In contrast, the shape of some larger particles in the SZ suggests that smaller particles attach to larger particles, which should represent the mechanical agglomeration process aided by the material flow during FSW. Interestingly, some evidence of mechanical agglomeration of particles has been noted in the SZ as an irregular shape of particles as shown in Figure 7 (c). Hence, it can be argued that the mechanism responsible for particle coarsening in the SZ is caused by the mechanically driven mechanism (particle agglomeration) coupled with the kinetically driven mechanism (Ostwald ripening).

4.2 Hardness profile of FSWed APMTTM

Hardness profiles of FSWed steels vary depending on the process conditions, initial microstructure, and intrinsic properties of steels such as phase transformation during the thermal cycles, the presence of second phases or the specimen thickness. As reported in the other studies involving the similar class of materials [8, 12, 13, 16], the material underwent different types of microstructural evolution due to thermomechanical effect during FSW, i.e. particle dissolution/coarsening, phase

transformation, and grain refinement/coarsening. In this work, microhardness testing across the transverse cross section did not reveal any significant region-specific change. Martensitic transformation could lead to the hardness spike in the SZ or the HAZ, but in APMTTM steel the high concentration of Cr (ferrite phase stabilizer), low carbon content and minor alloying elements, such as Ti, having high affinity for interstitial elements, retain the ferritic matrix across all temperatures and prevent possibility of martensitic phase transformation during FSW. Optical microscopy revealed the difference in the grain size between the SZ and the BM. Hence, the similar hardness must have been an effect of balancing out of different strengthening contributions as will be discussed in the next section.

4.3 Strengthening mechanisms in the as-received and FSWed APMTTM

Strengthening mechanisms in materials can be understood in terms of the ability of obstacles to impede dislocation motion effectively. This ability is manifested in terms of higher yield strength. At ambient temperature, the dislocation movement is limited to dislocation gliding. Thus, the yield strength in APMTTM consists of individual contributions made by lattice friction stress (σ_O), solid solution strengthening (σ_{SS}), dislocation strengthening (σ_D), grain boundary strengthening (σ_{GB}), and particle strengthening (σ_P). Thus, yield strength of the material can be described by Equations (3) or (4) (i.e., linear summation or Pythagorean superposition) depending on the characteristics of the microstructural features contribution to the strengthening mechanism [30, 31].

$$\sigma_y = \sigma_O + \sigma_{SS} + \sigma_{GB} + \sigma_P + \sigma_D \quad (3)$$

$$\sigma_y = \sigma_O + \sigma_{SS} + \sigma_{GB} + (\sigma_P^2 + \sigma_D^2)^{1/2} \quad (4)$$

The first contribution in strengthening mechanism considered here is the Peierls-Nabarro stress (or lattice friction stress) that arises from the atomic attraction forces in the lattice. The stress required to move a dislocation on the slip plane along slip direction in a lattice is called Peierls-Nabarro stress (τ_p), which is the function of the dislocation width and lattice constant of particular material. Hence, the relationship can be written as [32]

$$\tau_p = \frac{2G}{1-\nu} \exp\left[-\frac{2\pi a}{(1-\nu)b}\right] \quad (5)$$

where a is the lattice parameter, b is the Burgers vector (0.248 nm) and ν is the Poisson ratio (0.33). The calculation of lattice friction from Equation (5) is rather difficult due to its dependence on dislocation characteristics (width of dislocation core, types of dislocation), which is outside the scope of this study. Thus, the reported (normal stress, σ_o) value (50 MPa) of ferritic lattice (BCC) in ferritic steels is used for our calculation here [33].

Solid solution strengthening is a hardening mechanism created by interstitial and/or substitutional solutes. Solutes in the solvent lattice introduce lattice strain fields that start to interact with the mobile

dislocations. Contributions from the alloying elements present are shown in Table III. The total solid solution strengthening contribution to yield strength from each alloying element is described by Equation (6).

$$\sigma_{SS} = \sum A_i C_i \quad (6)$$

where A_i is the strengthening coefficient of the alloying elements shown in Table III, and C_i is concentration of the i -th element (in wt%). Some strengthening coefficients of the elements are reported elsewhere [30, 34, 35]. The contributions from minor elements (Z, Hf, Y) are not taken into account as they mainly form second phase particles. Also, the same rationale is applied to Ti, C, and N. Regardless strength contributions from the solid solution strengthening appears to be significant (395 MPa in both the BM and the SZ).

Table III. Strengthening coefficients of alloying elements in ferritic steels and concentrations of alloying elements in Kanthal APMTTM

Element	Strengthening coefficient, A_i (MPa/wt%)	Concentration in APMT TM (wt%)
Cr	8.5 ^[30]	22
Si	83 ^[34]	0.7 (max)
Mo	57.3 ^[35]	3
Mn	37 ^[34]	0.4 (max)

Grain boundaries impede dislocation movement and create dislocation pile-ups. The strengthening mechanism by grain boundary strengthening follows the well-known Hall-Petch relation, which is of the form shown in Equation (7). Yield strength becomes higher as the grain size becomes smaller and vice versa. Although some subgrains could be observed in the BM, the contribution via subgrain strengthening is not taken into account here due to the irregular occurrence of those features.

$$\sigma_{GB} = k_{HP} d^{-1/2} \quad (7)$$

where k_{HP} is the unpinning constant and d is the grain diameter. The value of k is reported to be 15.9 MPa·mm^{1/2} [30]. Thus, the yield strength contributed by the Hall-Petch strengthening effect is calculated to be 59 MPa in the BM and 122 MPa in the SZ.

In particle-strengthened alloys, particle strengthening mechanism is deemed important. The second phase particles distributed within the matrix serve as obstacles to the movement of dislocations. In this study, the mean size of the particles is found to be rather large (106 nm in the BM and 147 nm in the SZ). Hence, the Orowan-Ashby equation (Equation 8), a modification to the original Orowan particle bypassing equation, is used here to determine the strength contribution [36].

$$\sigma_{P(Orowan-Ashby)} = \frac{0.538Gb\sqrt{f}}{d} \ln\left(\frac{d}{2b}\right) \quad (8)$$

where d is mean particle diameter in μm , and f is volume fraction of the particles in the matrix. The respective particle sizes and volume fractions are taken from Table I. The calculated σ_P values are calculated to be 51 MPa in the BM and 42 MPa in the SZ. The contribution of the second phase particles to room temperature yield strength is noticeably small even though APMTTM is called a dispersion strengthened alloy. Nevertheless, these particles help in imparting the high temperature strength of the alloy because their stability at elevated temperatures and may have important role to play under such conditions.

Dislocations strengthening or work hardening (σ_D) is generally created by the interactions between dislocations. The corresponding equation giving the relationship between the increased yield strength and dislocation density can be described by the following equation:

$$\sigma_D = M\alpha Gb\rho^{1/2} \quad (9)$$

where M is the Taylor factor of the polycrystalline material (2.733 for BCC [37]), G is the shear modulus of the steel, b is the Burgers vector, ρ is dislocation density, and α is a constant, reported to be about 0.5 [27]. Shear modulus and Burgers vector used in this work are taken as 60 GPa [38] and 0.248 nm. The dislocation strengthening values are calculated to be 44 MPa in the BM and 31 MPa in the SZ.

Contributions of these strengthening mechanisms following two different models, i.e. linear superposition (model 1), and quadratic superposition model (model 2). While adding all the strengthening contributions by using linear superposition relation (Equation 3), the yield strength is predicted to be 599 MPa in the BM and 640 MPa in the SZ. On the other hand, the yield strength calculated from the quadratic superposition model (Equation 4) was determined to be 571 MPa for BM and 619 MPa for SZ. Both models show the predicted strength values within 3.5% because neither the particle strengthening nor the dislocation strengthening predominates in the strengthening calculations. These values agree well with the experimentally measured yield strength data in the longitudinal direction within just 3% variation (see Table IV). Although the particle size and the grain size are the same in the SZ_(transverse) and the SZ_(longitudinal), the texture evolution during FSW likely played a role in increasing the yield strength along the longitudinal direction compared to the yield strength in the transverse direction. Since in our predictive analysis no texture effect was taken into account, the predicted longitudinal strength value did not show much difference from the transverse one. Detailed textural analysis is needed in order to explain the difference and will be investigated in the future.

Table IV. Contributions of various strengthening mechanisms to yield strength of FSW APMTTM
(note that all strength values listed in the table are in MPa)

Region	σ_O	σ_{SS}	σ_{GB}	σ_P	σ_D	$\sigma_{y(model\ 1)}$	$\sigma_{y(model\ 2)}$	$\sigma_{y(experiment)}$
BM _{model, transverse}	50	395	59	51	44	599	571	594
SZ _{model, transverse}	50	395	122	42	31	640	619	657
SZ _{model, longitudinal}	50	395	122	42	31	640	619	790

Despite the Vickers hardness being similar between the BM and the SZ regions (as shown in Figure 6), the yield strength values of both regions did exhibit somewhat discernible difference. Thus, while Vickers microhardness can provide adequate information on a localized scale, it is not sufficient alone to precisely express bulk mechanical behavior of the weld [39]. Therefore, tensile testing is an essential tool in order to obtain quantitative results on the mechanical properties from both engineering and scientific perspectives.

5. Conclusion

The conclusions drawn from the present study are summarized below.

- FSW modified the typical hot rolled microstructure of the APMTTM plate into a fine grained microstructure via dynamic recrystallization in the stir zone because of the high strain rate and heat input.
- Upon FSW, the original second particles in the alloy underwent some degree of coarsening, which is attributed to both mechanically driven particle agglomeration and kinetically driven Ostwald ripening.
- FSW improved the room temperature tensile properties (in the longitudinal direction) of the APMTTM plate in terms of yield strength, tensile strength and percentage elongation to fracture. However, the strength values of the SZ in the transverse direction were similar to those of the base material, following the trend in the microhardness, while the ductility improved in the transverse direction as well.
- FSW appears to be a promising technique for joining high chromium dispersion strengthened ferritic stainless steel Kanthal APMTTM or similar alloys. The weld efficiency (i.e. the strength ratio between strength of SZ and BM) calculated was close to 100% or better as observed from the Vickers microhardness and tensile testing results. Further extensive studies will be needed to qualify the FSW technique and APMTTM material for nuclear applications.

Acknowledgement

The material used in this work was procured by using funds from a project funded by the Nuclear Energy University Programs (NEUP). Also, Anumat Sittiho would like to acknowledge The Royal Thai Navy for providing him with a graduate scholarship. Finally, we would like to thank the reviewers for their thoughtful comments.

Data Availability Statement

The raw data required to reproduce these findings are available to download from the supported data repository of the Journal of Nuclear Materials.

References

- [1] S.J. Zinkle, K.A. Terrani, J.C. Gehin, L.J. Ott, L.L. Snead, Accident tolerant fuels for LWRs: A perspective, *J. Nucl. Mater.* 448 (2014) 374-379. <https://doi.org/10.1016/j.jnucmat.2013.12.005>
- [2] I. Charit, Accident tolerant nuclear fuels and cladding materials, *JOM* 70 (2018) 173–175. <https://doi.org/10.1007/s11837-017-2701-3>
- [3] Y. Yano, T. Tanno, H. Oka, S. Ohtsuka, T. Inoue, S. Kato, T. Torimaru, Ultra-high temperature tensile properties of ODS steel claddings under severe accident conditions, *J. Nucl. Mater.* 487 (2017) 229–237. <https://doi.org/10.1016/j.jnucmat.2017.02.021>
- [4] Z.G. Zhang, F. Gesmundo, P.Y. Hou, Y. Niu, Criteria for the formation of protective Al₂O₃ scales on Fe–Al and Fe–Cr–Al alloys. *Corros. Sci.* 48(3) (2006) 741-765. <https://doi.org/10.1016/j.corsci.2005.01.012>
- [5] B. Jönsson, Q. Lu, D. Chandrasekaran, R. Berglund, F. Rave, Oxidation and creep limited lifetime of Kanthal APMT®, a dispersion strengthened FeCrAlMo alloy designed for strength and oxidation resistance at high temperatures. *Oxid. Met.* 79 (1–2) (2013) 29–39. <https://doi.org/10.1007/s11085-012-9324-4>
- [6] Y. Yamamoto, B.A. Pint, K.A. Terrani, K.G. Field, Y. Yang, L.L. Snead, Development and property evaluation of nuclear grade wrought FeCrAl fuel cladding for light water reactors. *J. Nucl. Mater.* 467 (2015) 703–716. <https://doi.org/10.1016/j.jnucmat.2015.10.019>
- [7] J.R. Regina, J.N. Dupont, A.R. Marder, The effect of chromium on the weldability and microstructure of Fe–Cr–Al weld cladding, *Weld. J.* 86(6) (2007) 170-178.
- [8] P. Miao, G. Odette, J. Gould, J. Bernath, R. Miller, M. Alinger, C. Zanis, The microstructure and strength properties of MA957 nanostructured ferritic alloy joints produced by friction stir and electro-spark deposition welding, *J. Nucl. Mater.* 367-370 (2007) 1197-1202. <https://doi.org/10.1016/j.jnucmat.2007.03.232>

- [9] W.M. Thomas, E.D. Nicolas, E. D., J.C. Needham, M.G. Murch, P. Temple-Smith, C.J. Dawes, U.S. Patent No. 5460317, 1995, Washington, DC, U.S. Patent and Trademark Office.
- [10] R. Nandan, G.G. Roy, T.J. Lienert, T. Debroy, Three-dimensional heat and material flow during friction stir welding of mild steel, *Acta Mater.* 55(3) (2007) 883–895.
<https://doi.org/10.1016/j.actamat.2006.09.009>
- [11] H. Cho, S. Hong, J. Roh, H. Choi, S. Kang, R. Steel, H. Han, Three-dimensional numerical and experimental investigation on friction stir welding processes of ferritic stainless steel, *Acta Mater.* 61(7) (2013) 2649–2661. <https://doi.org/10.1016/j.actamat.2013.01.045>
- [12] K. Dawson, S. Cater, G.J. Tatlock, C. Stanhope, Friction stir welding of PM2000 ODS alloy, *Mater. Sci. Technol.* 30(13) (2014) 1685–1690.
<https://doi.org/10.1179/1743284714Y.0000000553>
- [13] S.H.C. Park, T. Kumagai, Y.S. Sato, H. Kokawa, K. Okamoto, S. Hirano, M. Inagaki, Microstructure and mechanical properties of friction stir welded 430 stainless steel, *Proceedings of the Fifteenth International Offshore and Polar Engineering Conference*, The International Society of Offshore and Polar Engineers, Seoul, Korea, June 19-24, 2005, pp. 6-12.
- [14] J. Han, H. Li, Z. Zhu, F. Barbaro, L. Jiang, H. Xu, L. Ma, Microstructure and mechanical properties of friction stir welded 18Cr–2Mo ferritic stainless steel thick plate. *Mater. Des.* 63 (2014) 238–246. <https://doi.org/10.1016/j.matdes.2014.05.070>
- [15] B. Mazumder, X. Yu, P.D. Edmondson, C.M. Parish, M.K. Miller, H.M. Meyer, Z. Feng, Effect of friction stir welding and post-weld heat treatment on a nanostructured ferritic alloy, *J. Nucl. Mater.* 469 (2016) 200–208. <https://doi.org/10.1016/j.jnucmat.2015.11.061>
- [16] B. Baker, K. Knippling, L. Brewer, Oxide particle growth during friction stir welding of fine grain MA956 oxide dispersion-strengthened steel, *Metall. Mater. Trans. E* 4(1) (2017) 1–12.
<https://doi.org/10.1007/s40553-016-0101-1>
- [17] M.H. Mathon, V. Klosek, Y. De Carlan, L. Forest, Study of PM2000 microstructure evolution following FSW process, *J. Nucl. Mater.* 386 (2009) 475–478.
<https://doi.org/10.1016/j.jnucmat.2008.12.163>
- [18] G. Grant, S. Weil, “*Friction Stir Welding of ODS Steels – Steps toward a Commercial Process*” (National Energy Technology Laboratory Report, 2010),
https://www.netl.doe.gov/File%20Library/Events/2010/ods/Glenn_Grant_FSW.pdf. Accessed September 12th, 2016.
- [19] A. Sittiho, V. Tungala, I. Charit, R.S. Mishra, Understanding Microstructure and Mechanical Properties of Friction Stir Processed Aluminum-Bearing High-Chromium Ferritic Stainless Steel,

- in: I. Charit, Y.T. Zhu, S.A. Maloy, P.K. Liaw (Eds.), *Mechanical and Creep Behavior of Advanced Materials*, Springer, Switzerland, 2017, pp. 263-272. https://doi.org/10.1007/978-3-319-51097-2_21
- [20] R.L. Higginson, C.M. Sellars, C. M. Worked Examples in Quantitative Metallography (Vol. 788), Maney Publishers, London, UK, 2003.
- [21] D. Delille, R. Pantel, E. Van Cappellen, Crystal thickness and extinction distance determination using energy filtered CBED pattern intensity measurement and dynamical diffraction theory fitting, *Ultramicroscopy* 87(1) (2001) 5-18. [https://doi.org/10.1016/S0304-3991\(00\)00067-X](https://doi.org/10.1016/S0304-3991(00)00067-X)
- [22] J. Engkvist, S. Canovic, K. Hellström, A. Järnäs, J.E. Svensson, L.G. Johansson, M. Halvarsson, Alumina scale formation on a powder metallurgical FeAl alloy (Kanthal APMT) at 900–1,100 °C in dry O₂ and in O₂+ H₂O, *Oxid. Met.* 73(1-2) (2010) 233-253. <https://doi.org/10.1007/s11085-009-9177-7>
- [23] C. Zener, J.H. Hollomon, Effect of strain rate upon plastic flow of steel, *J. Appl. Phys.* 15(1) (1944) 22-32. <https://doi.org/10.1063/1.1707363>
- [24] A. H. Ammouri, G. Kridli, G. Ayoub, R.F. Hamade, Relating grain size to the Zener–Hollomon parameter for twin-roll-cast AZ31B alloy refined by friction stir processing, *J. Mater. Process. Technol.* 222 (2015) 301-306. <https://doi.org/10.1016/j.jmatprotec.2015.02.037>
- [25] S. Palanivel, A. Arora, K.J. Doherty, R.S. Mishra, A framework for shear driven dissolution of thermally stable particles during friction stir welding and processing, *Mater. Sci. Eng. A* 678 (2016) 308-314. <https://doi.org/10.1016/j.msea.2016.10.015>
- [26] J. Wang, W. Yuan, R.S. Mishra, I. Charit, Microstructural evolution and mechanical properties of friction stir welded ODS alloy MA754, *J. Nucl. Mater.* 442(1) (2013) 1-6. <https://doi.org/10.1016/j.jnucmat.2013.08.012>
- [27] M.J. Bird, Oxide evolution in ODS steel resulting from friction stir welding, Master's thesis, Naval Postgraduate School, Monterey, CA, 2014.
- [28] B. Baker, Processing, microstructure, and material property relationships following friction stir welding of oxide dispersion strengthened steels, PhD dissertation, Naval Postgraduate School, Monterey, CA, 2013.
- [29] R.W. Balluffi, S. Allen, W.C. Carter, *Kinetics of Materials*, John Wiley & Sons, Hoboken, New Jersey, USA, 2005.
- [30] J. Wang, W. Yuan, R.S. Mishra, Charit, I., Microstructure and mechanical properties of friction stir welded oxide dispersion strengthened alloy, *J. Nucl. Mater.* 432(1) (2013) 274-280. <https://doi.org/10.1016/j.jnucmat.2012.08.001>

- [31] S. Queyreau, G. Monnet, B. Devincere, Orowan strengthening and forest hardening superposition examined by dislocation dynamics simulations, *Acta Mater.* 58(17) (2010) 5586–5595.
<https://doi.org/10.1016/j.actamat.2010.06.028>
- [32] Dieter, G. E., & Bacon, D. J., *Mechanical Metallurgy*, Third ed., McGraw-Hill, New York, 1986.
- [33] W.C. Leslie, Iron and its dilute substitutional solid solutions, *Metall. Trans.* 3(1) (1972) 5-26.
<https://doi.org/10.1007/BF02680580>
- [34] G.E. Totten, L. Xie, K. Funatani, *Handbook of Mechanical Alloy Design*, Marcel Dekker, New York, USA, 2004.
- [35] A. Guria, I. Charit, Tensile properties of accident-tolerant aluminum-bearing ferritic steels, *Ann. Nucl. Energy* 100 (2017) 82-88. <https://doi.org/10.1016/j.anucene.2016.09.018>
- [36] J. Fu, G. Li, X. Mao, K. Fang, Nanoscale cementite precipitates and comprehensive strengthening mechanism of steel, *Metall. Mater. Trans. A* 42(12) (2011), 3797-3812.
<https://doi.org/10.1007/s11661-011-0767-z>
- [37] J.M. Rosenberg, H.R. Piehler, Calculation of the Taylor factor and lattice rotations for bcc metals deforming by pencil glide, *Metall. Trans.* 2(1) (1971) 257-259. <https://doi.org/10.1007/BF02662666>
- [38] A. Wasilkowska, M. Bartsch, U. Messerschmidt, R. Herzog, A. Czyrska-Filemonowicz, Creep mechanisms of ferritic oxide dispersion strengthened alloys, *J. Mater. Process. Technol.* 133(1) (2003) 218–224. [https://doi.org/10.1016/S0924-0136\(02\)00237-6](https://doi.org/10.1016/S0924-0136(02)00237-6)
- [39] E.J. Pavlina, C.J. Van Tyne, Correlation of yield strength and tensile strength with hardness for steels. *J. Mater. Eng. Perform.*, 17(6) (2008) 888–893. <https://doi.org/10.1007/s11665-008-9225-5>